

## 2D MATERIALS

# High-temperature quantum valley Hall effect with quantized resistance and a topological switch

Ke Huang<sup>1</sup>, Hailong Fu<sup>1†</sup>, Kenji Watanabe<sup>2</sup>, Takashi Taniguchi<sup>3</sup>, Jun Zhu<sup>1,4\*</sup>

Edge states of a topological insulator can be used to explore fundamental science emerging at the interface of low dimensionality and topology. Achieving a robust conductance quantization, however, has proven challenging for helical edge states. In this work, we show wide resistance plateaus in kink states—a manifestation of the quantum valley Hall effect in Bernal bilayer graphene—quantized to the predicted value at zero magnetic field. The plateau resistance has a very weak temperature dependence up to 50 kelvin and is flat within a dc bias window of tens of millivolts. We demonstrate the electrical operation of a topology-controlled switch with an on/off ratio of 200. These results demonstrate the robustness and tunability of the kink states and its promise in constructing electron quantum optics devices.

Chiral and helical edge states arising from a nontrivial bulk topology are expected to be protected against backscattering and support a wealth of interesting topological, mesoscopic, and interacting phenomena in low dimensions (1, 2). Chiral edge states of the quantum Hall (QH) and quantum anomalous Hall (QAH) effects are ballistic over long distances (1, 3–6), harbor the physics of a chiral Luttinger liquid (7), and are instrumental to the understanding of fractional and non-Abelian braiding statistics (8, 9). Helical edge states of the quantum spin Hall (QSH) and quantum valley Hall (QVH) effects occur at zero external and internal magnetic field, which is generally more compatible with device applications (10–28). Previously, QVH internal edge states, known as the kink states, were realized in Bernal bilayer graphene (BLG) using lithographically patterned gates, and operations of a valley valve and electron beam splitter were demonstrated (22, 23). The tunable beam splitter is analogous to the action of a quantum point contact, which is a powerful element used in a wide range of fundamental research and quantum devices (29). The absence of precise resistance quantization, which implies that backscattering is still present, is a critical impediment to the pursuit of some of the most exciting prospects of helical one-dimensional (1D) systems, such as topological superconductivity (27, 28, 30, 31), helical Luttinger liquid physics (13, 32–34), and the development of edge-based quantum transport devices (11, 18, 23, 28, 35).

In this study, we report on the precise quantization of QVH kink state resistance to better than 1% of the expected  $R = h/4e^2 = 6453$  ohms (where  $h$  is the Planck's constant and  $e$  is the elementary electron charge) at zero magnetic field and its persistence to tens of kelvin. We further demonstrate the fast and repeatable operation of a topological switch, the mechanism of which is based on an electric field-controlled topological phase transition specific to the kink states. The ballistic transport, in situ programmability, and scalable fabrication of the kink states lay a strong foundation for future studies exploring the fundamental science and application potentials of this helical 1D system.

## Device structure and characterization

Figure 1, A and B, illustrates the topological origin of the QVH effect in BLG (16–20) and a dual split gate-based experimental scheme, respectively (16, 22–24, 26). The four split gates—i.e., the left/right top/bottom gates (L/R T/B Gs)—define two independently gated regions. We induce bulk gaps of opposite sign in the two regions, and the resulting band inversion at the nanoribbon junction creates valley momentum-locked kink states inside the junction. The device structure in Fig. 1B enables electrical control of the transition between the topological phase with the existence of the kink states and the trivial phase without it. This situation is illustrated in Fig. 1C and underlies the working mechanism of a topological switch (11), which we will demonstrate. Each valley (K and K') contains four chiral modes. Ballistic transport of the kink states results in a two-terminal junction resistance of  $h/4e^2 = 6453$  ohms. Electron backscattering requires an intervalley scattering that involves a large momentum transfer of order  $[(\text{lattice constant})^{-1}]$ ; such events are highly suppressed in highly crystalline BLG but not completely absent because of residual Coulomb impurities. The mean free path of the kink

states is at most a few micrometers in previous experiments, and the zero-field resistance is at least hundreds of ohms away from  $h/4e^2$  with no clear quantization plateaus (21–24, 26).

The key technical advance of this work is the incorporation of a graphite/hexagonal boron nitride (h-BN) stack as a global gate (GG) to tune the Fermi level of the kink states. Previous devices (22, 23) used a doped Si/SiO<sub>2</sub> stack, which was shown to be an important source of potential disorder (36). We use dry van der Waals transfer, annealing, and reactive ion etching to create the graphite split LBG and RBG, an atomic force microscope (AFM) image of which is shown in Fig. 1E. Additional transfers and e-beam lithography are used to complete the device (figs. S1 to S3) (37). Figure 1D shows a false-color scanning electron microscope (SEM) image of K23 with a 61-nm-wide, 400-nm-long junction. The two-terminal resistance of the junction  $R = R_k + R_c$  includes both the kink state resistance  $R_k$  and the contact resistance  $R_c$ ;  $R_c$  is accurately determined using the resistance quantization of the QH effect (Fig. 2C) and is typically a few hundred ohms.

We characterize the five gates (LTG, LBG, RTG, RBG, and GG) (fig. S4) and place the dual-gated areas (shaded gold in Fig. 1D) in the middle of a  $D$  field-induced bulk gap  $\Delta$ , with a typical size of tens of milli-electron volts. Figure 1F shows the evolution of the junction resistance  $R$  in device K22 as the device is tuned from the “–” gating configuration (both left and right  $D$  fields pointing down) to the “+” configuration (left down, right up).  $R$  reaches megohms in the “–” configuration, where the residual conductance comes from localized states in the nanoribbon junction (22, 23). It saturates to 6 to 7 kilohms in the “+” configuration, which confirms the presence of the kink states in the topological regime.

## Resistance quantization at $B = 0$ T

We apply a voltage to the GG,  $V_{GG}$ , to tune the Fermi level  $E_F$  inside the junction. Figure 2A plots an example of the junction resistance  $R$  ( $V_{GG}$ ) in device K22. Inside the gap, where only the kink states are present,  $R$  exhibits a flat resistance plateau of  $R = (6557 \pm 12)$  ohms. Similar plateaus, with  $R$  very close to the expected  $h/4e^2$ , are observed at other  $D$  fields [see fig. S5 for a systematic investigation of  $R(V_{GG})$  under different  $D$  fields]. Excellent resistance quantization is also observed in other devices. Figure 2B plots a few exemplary  $R(V_{GG})$  traces in K24, and measurements in WK05 are given in fig. S7.

The breaking of time-reversal symmetry through the application of a magnetic field does not destroy the kink states (19, 22, 23). Indeed, our measurements show that  $R$  only varies by 53 ohms from 0 to 9 T, likely owing to small changes in  $R_c$  (fig. S6B). As the  $B$  field increases, the conduction and valence bands

<sup>1</sup>Department of Physics, The Pennsylvania State University, University Park, PA 16802, USA. <sup>2</sup>Research Center for Electronic and Optical Materials, National Institute for Materials Science, 1-1 Namiki, Tsukuba 305-0044, Japan. <sup>3</sup>Research Center for Materials Nanoarchitectonics, National Institute for Materials Science, 1-1 Namiki, Tsukuba 305-0044, Japan. <sup>4</sup>Center for 2-Dimensional and Layered Materials, The Pennsylvania State University, University Park, PA 16802, USA.

\*Corresponding author. Email: jzhu@phys.psu.edu

†Present address: School of Physics, Zhejiang University, Hangzhou 310058, China.

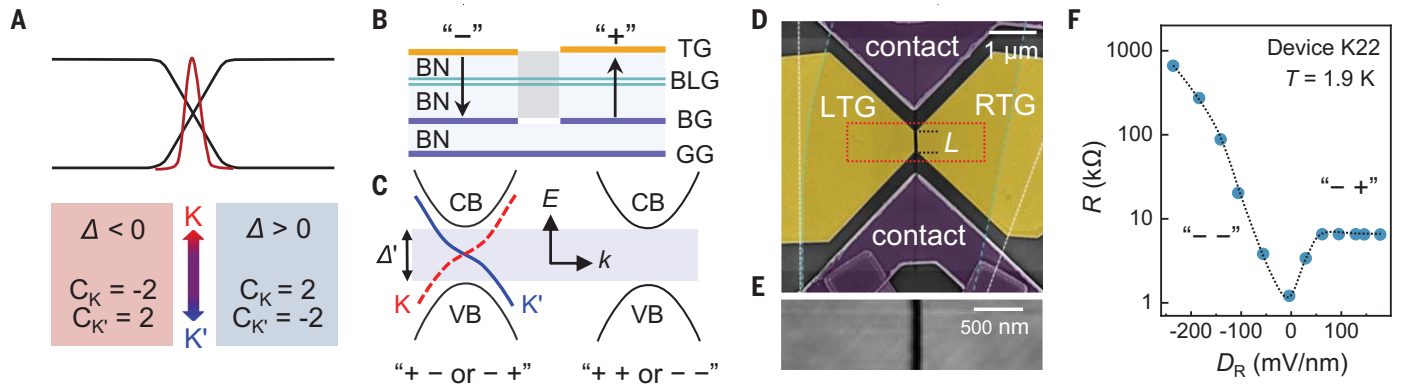


**Fig. 1. The QVH kink states in bilayer graphene.** (A) Schematic band diagram showing the inverted bands, the wave function of the kink states, and its topological origin. The valley Chern number changes by  $+4/-4$  in the  $K/K'$  valley across the junction, giving rise to four chiral modes in each valley. (B) Schematic side view of our device structure. The  $D$  field points up in a “+” configuration. (C) 1D band diagram of the junction [gray area in (B)] in the “+ - or - +” (topological) or “+ + or - -” (trivial) gating configurations. CB, conduction band; VB, valence band. (D) A false-color SEM image of device K23. The Ti/Au top split gates align with the graphite bottom split gates. The BLG sheet is

outlined in cyan, and the global graphite gate is outlined in white. The side contacts are colored purple. They contact the kink states through the heavily doped access region at the two ends. The junction length  $L = 400$  nm in all our devices. (E) An AFM image of the 61-nm-wide bottom graphite split gates in the area enclosed by the red box in (D). The surface is clean after annealing. In devices K22, K24, and WK05, the widths are 74, 71, and 74 nm, respectively. (F) The junction resistance  $R$  in device K22 as a function of  $D_R$ .  $D_L = -161$  mV/nm.  $B = 0$  T.  $T = 1.9$  K. The data are extracted from fig. S5B. See (37) for the fabrication and characterization of the devices.  $\Omega$ , ohm.

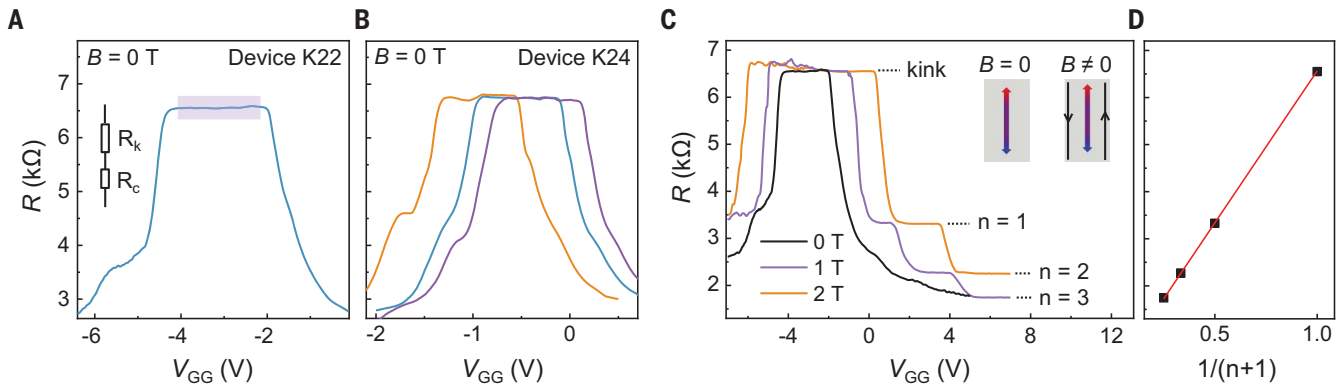


**Fig. 2. The resistance quantization of the kink states.** (A) Junction resistance  $R$  versus  $V_{GG}$  in device K22. In the purple-shaded region,  $R = 6557 \pm 12$  ohms. (B)  $R(V_{GG})$  at selected  $D_L$  values in K24.  $D_L = -296$  (orange),  $-199$  (blue), and  $-150$  (violet) mV/nm.  $D_R = 241$  mV/nm for all. The traces are shifted in  $V_{GG}$  owing to misalignment on the left gates.  $B = 0$  T for both (A) and (B). (C)  $R(V_{GG})$  at selected magnetic fields, as labeled in the graph. (Inset)

Illustration of the appearance of QH edge states in the nanoribbon junction in a finite  $B$  field. The index  $n$  marks the number of occupied LLs. (D)  $R$  versus  $1/(n+1)$ . Points are taken from the data at 1 T in (C). A linear fit (red line) using Eq. 1 yields  $R_c = 114$  ohms and  $R_k = 6443$  ohms. (A), (C), and (D) are from device K22 with  $D_L = -161$  mV/nm and  $D_R = 146$  mV/nm.  $T = 1.9$  K for all data in this figure.

of the nanoribbon junction evolve into Landau levels (LLs), with each LL contributing  $4e^2/h$  to the total conductance. Thus, the total junction resistance is

$$R = R_c + \frac{h}{4e^2(1+n)} \quad (1)$$

where  $n = 0, 1, 2, \dots$  represents the kink only ( $n = 0$ ) and the number of occupied LLs. The main panel of Fig. 2C shows the measured  $R(V_{GG})$  at  $B = 0, 1$ , and  $2$  T, with the LL quantization already well developed at  $B = 1$  T. The measured  $R$  values are extremely well described by Eq. 1, and a linear fit to the  $B = 1$  T data (Fig. 2D) yields  $R_c = 114$  ohms and  $R_k = R - R_c = 6443$  ohms.  $R_k$  deviates from the

expected value of  $h/4e^2 = 6453$  ohms by 10 ohms. Performing similar analysis at other  $B$  fields and temperatures, we find the resulting  $R_k$  to always fall within 0.4% of  $h/4e^2$  (table S3). We have also examined the variations of the kink state plateau resistance at different  $D$  and  $B$  fields in multiple devices (figs. S5 to S7). These analyses allowed us to place 1% as an upper bound to the accuracy of  $R_k$  in our experiment. Our results unambiguously demonstrate the precise and robust quantization of the kink state resistance. Quantization to this level has so far only been observed in chiral edge states ( $1, 3, 5$ ), whereas helical edge states in any materials are more vulnerable to backscattering. The excellent ballisticity and scalability

of the QVH kink states make it an attractive platform to construct electronic waveguides and explore quantum information concepts, such as a flying qubit (38).

### The temperature dependence

The temperature dependence of the kink states is examined in Fig. 3. Figure 3A plots exemplary  $T$ -dependent  $R(V_{GG})$  traces taken in device K22. The junction resistance  $R$  remains constant at low temperatures and decreases slowly with increasing  $T$ . Figure 3B plots the normalized plateau center resistance  $R$  versus  $T$  at selected bulk  $D$  fields in K22 and WK05.  $R(T)$  has very weak  $T$  dependence, especially when  $D$ , hence the bulk gap  $\Delta$ , is large. Figure 3C

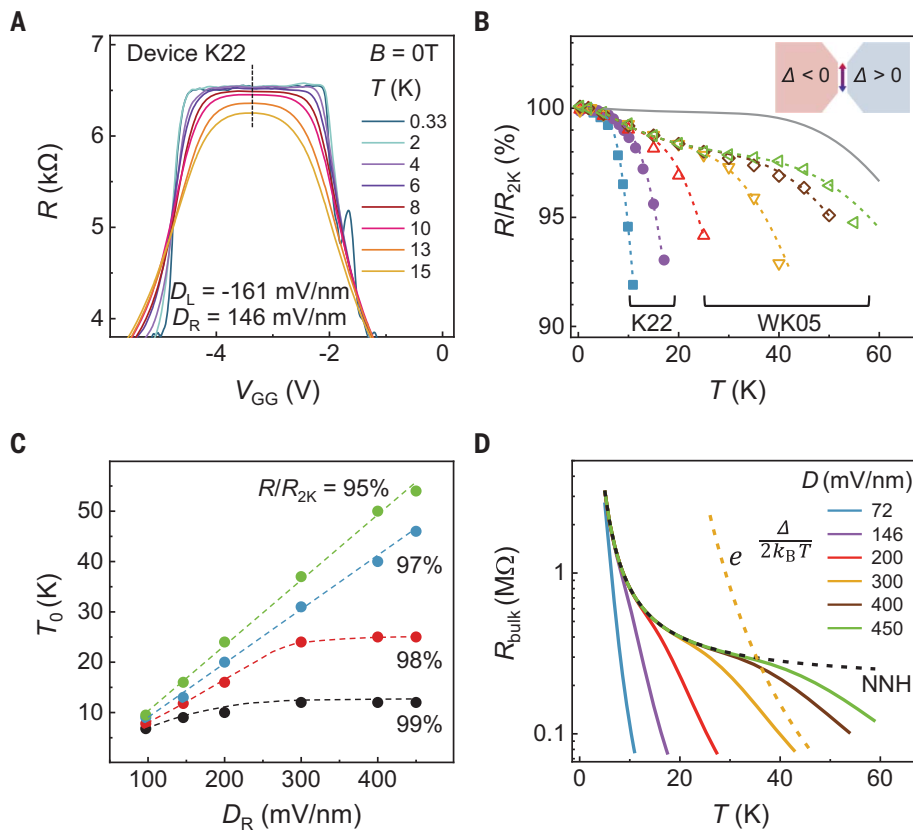


**Fig. 3. The temperature dependence of the junction resistance.** (A)  $R(V_{GG})$  measured in device K22 at temperatures from 0.33 K to 15 K, as labeled in the graph. (B) Normalized plateau center resistance  $R/R(T = 2 \text{ K})$  versus  $T$  at selected  $D$  values. Solid symbols are from device K22, where  $D_L = -161 \text{ mV/nm}$  is fixed, and  $D_R$  changes in this device. Open symbols are from device WK05, where  $D_L = -D_R$ . The  $D_R$  values of both solid and open symbols follow the legend in (D). Raw data in WK05 are shown in fig. S7. The dashed lines plot  $R = R_{2K}R_{\text{bulk}}(T)/[R_{2K} + R_{\text{bulk}}(T)]$ , where  $R_{\text{bulk}}(T)$  is given by Eq. 2 and plotted in (D). (Inset) Illustration of the parallel bulk and kink state contributions to  $R$ .  $B = 0 \text{ T}$  for all data in this figure. (C) Temperatures  $T_0$  at which  $R/R_{2K} = 95\%$ ,  $97\%$ ,  $98\%$ , and  $99\%$ , using measurements in (B). Dashed lines are provided to guide the eye. (D) Simulated bulk resistance  $R_{\text{bulk}}(T)$  using Eq. 2 for different  $D$  fields, as labeled in the graph. The orange and black dashed lines plot the thermally activated and the NNH terms separately for the orange trace. The two traces cross at 35 K. The total  $R_{\text{bulk}}(T)$  is dominated by thermal activation above 35 K and NNH below 35 K. The expanding dominance of NNH at large  $D$  values leads to a saturated  $R_{\text{bulk}}$  and a shoulder-like feature in  $R/R_{2K}$  in (B). The gray solid line in (B) plots a simulated scenario, where the NNH resistance in the green dashed line is increased 10-fold through, for example, reducing the number of impurity states or reducing the width of the gapped bulk. In this scenario, the contribution of  $R_{\text{bulk}}$  becomes negligible below 40 K.

plots the temperature  $T_0$  at which  $R$  deviates from its low- $T$  value by 1, 2, 3, and 5%. Notably, at  $D = 450 \text{ mV/nm}$  or  $\Delta \sim 58 \text{ meV}$  (39),  $T_0 = 12 \text{ K}$  for 1% and 46 K for 3%. This high level of  $T$  independence is a hallmark of topological edge states but has only been observed previously in the QH effect, whereas QAH and QSH systems appear to be more vulnerable to temperature (3–6, 10, 12, 14, 40, 41).

The complex behavior of  $R(T)$  shown in Fig. 3B can in fact be well explained by recognizing the fact that the gapped BLG bulk conducts in parallel to the kink states, as the inset illustrates. In this temperature range, the  $T$  dependence of gapped BLG is well understood as

consisting of thermally activated band transport and nearest neighbor hopping (NNH) inside the gap, that is

$$R_{\text{bulk}}^{-1} = R_1^{-1}e^{(-\Delta/2k_B T)} + R_2^{-1}e^{(-E_2/k_B T)} \quad (2)$$

where  $R_1$  and  $R_2$  are constants,  $E_2$  is the average energy difference between adjacent impurity sites, and  $k_B$  is the Boltzmann constant (39, 42–45). Figure 3D plots the simulated  $R_{\text{bulk}}(T)$  using  $R_1 = 1 \text{ kilohm}$ ,  $R_2 = 200 \text{ kilohms}$ ,  $E_2 = 1.2 \text{ meV}$ , and  $\Delta$  (in milli-electron volts) =  $-5.7 + 0.13D$  (in millivolts per nanometer) [see section S6 of (37)]. The simulated total junction resistance  $R = R_{2K}/R_{\text{bulk}}$  is plotted in Fig.

3B as dashed lines and is in excellent agreement with the measured data. The fact that this simple model appears to have captured all of the complex features of the  $R(T)$  traces, qualitatively and quantitatively, gives us confidence in its validity.

The above analysis suggests that the intrinsic  $T$  dependence of the kink states remains undiscernible—i.e., phonon-assisted intervalley scattering is negligible, up to 50 K. We note that BLG phonons carrying the required intervalley momentum transfer  $\delta k$  of the 1D kink states have a minimum energy  $\hbar\omega_{\text{min}}$  as high as 68 meV when the junction aligns with the zigzag crystallographic orientation of the BLG (46, 47). When the junction deviates from the zigzag direction,  $\delta k$  is reduced but remains large [see section S3 of (37) for an estimate of  $\delta k$  in our devices]. Thus, the kink states may be immune to phonon-assisted backscattering to temperatures on the order of 100 K. The further suppression of bulk conduction—e.g., through increasing  $\Delta$  and reducing impurity sites—will enable us to fully examine its potential.

### The dc bias dependence

Next, we examined the dc bias dependence of the kink states. Figure 4A shows a false-color map of differential conductance  $G(V_{\text{dc}}, V_{GG})$  in device K22. Figure 4A is reminiscent of the transport spectroscopy of an insulator, only here  $G = 4e^2/h$  inside the diamond-like region. Figure 4B plots  $G(V_{\text{dc}})$  traces taken in WK05 with  $V_{GG}$  positioned at midgap and at selected  $D$  fields.  $G(V_{\text{dc}})$  is nearly flat at low biases and increases sharply at a bias threshold  $V_{\text{dc}}$ , which increases with increasing  $D$ .  $V_{\text{dc}}(D)$  determined from measurements is plotted in Fig. 4C. It exhibits an approximate linear dependence with a slope of  $0.09 \text{ mV/(mV/nm)}$  and reaches several tens of millivolts at large  $D$ . Our data can be well understood using the band diagram shown as the inset of Fig. 4C, where the sharp onset of  $G$  at  $V_{\text{dc}}$  corresponds to the electrochemical potential of the electrodes reaching the band edge of the nanoribbon junction. We obtain  $\Delta'$  (in milli-electron volts) =  $-4 + 0.09D$  (in millivolts per nanometer) from data, which is consistent with band structure simulations of a finite-width nanoribbon junction (22). The behavior of the kink states at finite dc biases attests to the cleanliness of the gapped region and further demonstrates the robust quantization of the kink states. The large bias window of several tens of millivolts facilitates potential single-electron manipulations.

### A topological switch

As illustrated in Fig. 1C, the kink state has a specific property—that is, its presence can be turned on and off using an electric field-controlled topological-to-trivial insulator transition. This topological phase transition-driven switch is

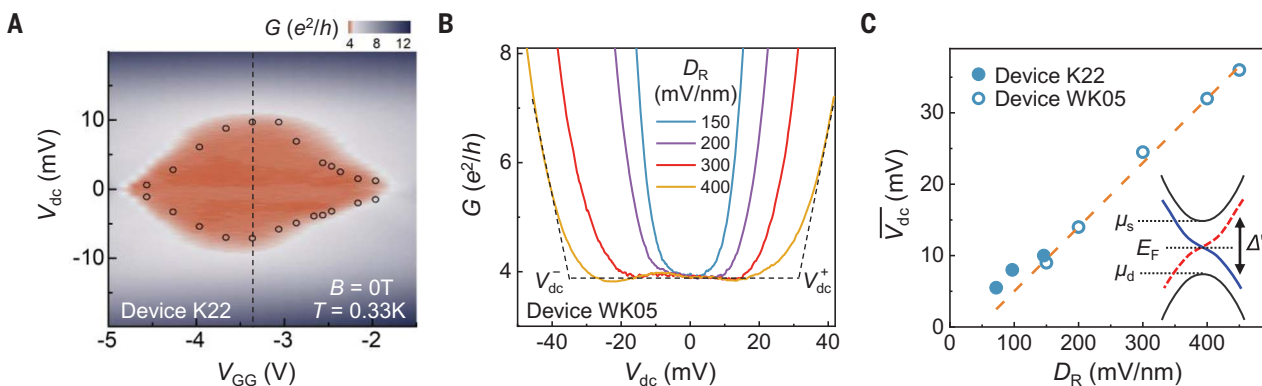


**Fig. 4. The dc bias dependence of the kink states.** (A) False-color map of differential conductance  $G(V_{dc}, V_{GG})$  in device K22.  $D_L = -161$  mV/nm and  $D_R = 146$  mV/nm. The onset of high conduction, defined as  $G = 4.3e^2/h$  (white color in the map) traces out a diamond-like shape. (B)  $G(V_{dc})$  sweeps obtained in device WK05 with  $E_F$  positioned at midgap and at selected  $D$  values, as labeled.  $D_L = -D_R$ . The black dashed lines illustrate a second way of defining the

conduction onset dc bias  $V_{dc}$ . Open circles in (A) are obtained using this method. (C) The average onset bias  $V_{dc}^- = (V_{dc}^+ - V_{dc}^-)/2$  as a function of  $D_R$  in both devices.  $D_L = -161$  mV/nm is fixed in K22.  $D_L = -D_R$  in WK05. (Inset) Illustration of the onset of band conduction at a finite dc bias  $eV_{dc} = \mu_s - \mu_d = \Delta'$ , where  $\Delta'$  is the band gap of the nanoribbon junction. The orange dashed line has a slope of 0.09 mV/(mV/nm).  $B = 0$  T and  $T = 0.33$  K for all data in this figure.

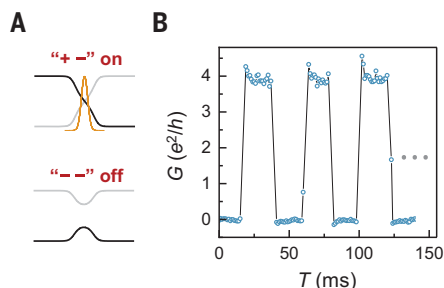


**Fig. 5. A topological phase transition-controlled switch.** (A) Band diagrams for the “on” (top) and “off” states (bottom) of the switch using calculations from Li *et al.* (22). (B) The operation of the switch for a few cycles.  $D_L = 57$  mV/nm ( $V_{LTG} = -1$  V,  $V_{LBG} = 0.467$  V) and  $-75$  mV/nm ( $V_{LTG} = 1$  V,  $V_{LBG} = -0.687$  V), respectively, for the on and off states.  $D_R$  is fixed at  $-170$  mV/nm. The on/off ratio is  $\sim 200$ .  $B = 0$  T and  $T = 0.33$  K. Figure S9 provides more examples of the switching operations of the junction.

fundamentally different from that of a conventional transistor, which operates through carrier concentration change. In the literature, topological switches based on phase transitions were proposed for QSH and topological crystalline insulators (11, 48), but these proposals are difficult to realize experimentally. Figure 5 shows the operations of our kink state topological switch, where the junction conductance is switched between  $\sim 4e^2/h$  and  $\sim 0$  repeatedly as the gating configurations are alternated between the “+ -” and “- -” configurations through the voltage swing of a few volts. This operation is very reproducible. The on/off ratio is  $\sim 200$ , which can be further increased by reducing the “off” state conductance. The rise time of  $\sim 6$  ms is limited by the charging speed of the gates. Neither param-

eter is limited by the intrinsic properties of the kink states, and both have much room for further improvement.

#### Discussion and outlook

In this work, we have achieved the quantization of the QVH effect at zero magnetic field and to high temperatures of tens of kelvin. Its manifestation in bilayer graphene—the kink state—distinguishes itself from other chiral and helical edge state systems in its electrical creation and wide in situ tunability, which make it an attractive platform to construct on-chip quantum electronics that mimic the functionalities of quantum optics. Clean material and device construction are crucial to the realization of this potential. Substantial improvement was made in this work, which led to excellent ballistic charge transport of the kink states and resistance quantization. This quantization is also robust in wide temperature and voltage ranges owing to relatively few in-gap states and the high energies of phonons in graphene. Our experiments point to lowering defect and charged impurity states as a vital path to achieving quantized transport, especially for helical edge states, where the wave functions of the time-reversed pair colocate spatially. We envision the construction of a quantum interconnect network using the kink states as the backbone and integrating the functional elements demonstrated to date, namely switch, waveguide, valve, and beam splitter (23). Such a network may be used to carry quantum information on-chip over a long distance, for which the preservation of quantum coherence and entanglement is essential. The demonstration of long spin relaxation length in bilayer graphene (49) bodes well for this vision; phase coherent transport is a promising direction to explore

(38). Kink states are also excellent candidates to explore the physics of 1D helical Luttinger liquid through tunneling experiments analogous to measurements performed for chiral edge states at a quantum point contact (7, 50). The helical nature of the edge states is expected to give rise to different critical behaviors (33). Coupling kink states to superconductivity is another interesting direction to pursue, and recent experiments using domain wall modes in twisted bilayer graphene have yielded promising initial results (51).

#### REFERENCES AND NOTES

- S. Das Sarma, A. Pinczuk, Eds., *Perspectives in Quantum Hall Effects: Novel Quantum Liquids in Low-Dimensional Semiconductor Structures* (Wiley, 1997).
- X.-L. Qi, S.-C. Zhang, *Rev. Mod. Phys.* **83**, 1057–1110 (2011).
- C.-Z. Chang *et al.*, *Science* **340**, 167–170 (2013).
- Y. Deng *et al.*, *Science* **367**, 895–900 (2020).
- M. Serlin *et al.*, *Science* **367**, 900–903 (2020).
- T. Li *et al.*, *Nature* **600**, 641–646 (2021).
- A. M. Chang, *Rev. Mod. Phys.* **75**, 1449–1505 (2003).
- C. Nayak, S. H. Simon, A. Stern, M. Freedman, S. Das Sarma, *Rev. Mod. Phys.* **80**, 1083–1159 (2008).
- J. Nakamura, S. Liang, G. C. Gardner, M. J. Manfra, *Nat. Phys.* **16**, 931–936 (2020).
- M. König *et al.*, *Science* **318**, 766–770 (2007).
- X. Qian, J. Liu, L. Fu, J. Li, *Science* **346**, 1344–1347 (2014).
- L. Du, I. Knez, G. Sullivan, R. R. Du, *Phys. Rev. Lett.* **114**, 096802 (2015).
- T. Li *et al.*, *Phys. Rev. Lett.* **115**, 136804 (2015).
- Z. Y. Fei *et al.*, *Nat. Phys.* **13**, 677–682 (2017).
- S. Wu *et al.*, *Science* **359**, 76–79 (2018).
- I. Martin, Y. M. Blanter, A. F. Morpurgo, *Phys. Rev. Lett.* **100**, 036804 (2008).
- J. Li, A. Morpurgo, M. Büttiker, I. Martin, *Phys. Rev. B* **82**, 245404 (2010).
- Z. Qiao, J. Jung, Q. Niu, A. H. MacDonald, *Nano Lett.* **11**, 3453–3459 (2011).
- M. Zarenia, J. M. Pereira, G. A. Farias, F. M. Peeters, *Phys. Rev. B* **84**, 125451 (2011).
- F. Zhang, A. H. MacDonald, E. J. Mele, *Proc. Natl. Acad. Sci. U.S.A.* **110**, 10546–10551 (2013).
- L. Ju *et al.*, *Nature* **520**, 650–655 (2015).
- J. Li *et al.*, *Nat. Nanotechnol.* **11**, 1060–1065 (2016).
- J. Li *et al.*, *Science* **362**, 1149–1152 (2018).
- J. Lee, K. Watanabe, T. Taniguchi, H. J. Lee, *Sci. Rep.* **7**, 6466 (2017).

25. E. Mania, A. R. Cadore, T. Taniguchi, K. Watanabe, L. C. Campos, *Commun. Phys.* **2**, 6 (2019).
26. H. Chen *et al.*, *Nat. Commun.* **11**, 1202 (2020).
27. S. Cheng *et al.*, *Phys. Rev. B* **101**, 165420 (2020).
28. M. S. Lodge, S. A. Yang, S. Mukherjee, B. Weber, *Adv. Mater.* **33**, e2008029 (2021).
29. H. van Houten, C. Beenakker, *Phys. Today* **49**, 22–27 (1996).
30. S. Hart *et al.*, *Nat. Phys.* **10**, 638–643 (2014).
31. E. Bocquillon *et al.*, *Nat. Nanotechnol.* **12**, 137–143 (2017).
32. M. Killi, T.-C. Wei, I. Affleck, A. Paramakanti, *Phys. Rev. Lett.* **104**, 216406 (2010).
33. B. J. Wieder, F. Zhang, C. L. Kane, *Phys. Rev. B* **92**, 085425 (2015).
34. R.-X. Zhang, C.-X. Liu, *Phys. Rev. Lett.* **118**, 216803 (2017).
35. A. C. Mahoney *et al.*, *Nat. Commun.* **8**, 1836 (2017).
36. D. Rhodes, S. H. Chae, R. Ribeiro-Palau, J. Hone, *Nat. Mater.* **18**, 541–549 (2019).
37. See the supplementary materials.
38. M. Yamamoto *et al.*, *Nat. Nanotechnol.* **7**, 247–251 (2012).
39. J. Li, Y. Tupikov, K. Watanabe, T. Taniguchi, J. Zhu, *Phys. Rev. Lett.* **120**, 047701 (2018).
40. H. P. Wei, A. M. Chang, D. C. Tsui, M. Razeghi, *Phys. Rev. B* **32**, 7016–7019 (1985).
41. K. S. Novoselov *et al.*, *Science* **315**, 1379–1379 (2007).
42. B. I. Shklovskii, A. L. Efros, *Electronic Properties of Doped Semiconductors* (Springer, 1984).
43. J. B. Oostinga, H. B. Heersche, X. Liu, A. F. Morpurgo, L. M. K. Vandersypen, *Nat. Mater.* **7**, 151–157 (2008).
44. T. Taychatanapat, P. Jarillo-Herrero, *Phys. Rev. Lett.* **105**, 166601 (2010).
45. K. Zou, J. Zhu, *Phys. Rev. B* **82**, 081407 (2010).
46. M. Kim *et al.*, *Nat. Phys.* **12**, 1022–1026 (2016).
47. D. L. Nika, A. A. Balandin, *Rep. Prog. Phys.* **80**, 036502 (2017).
48. J. Liu *et al.*, *Nat. Mater.* **13**, 178–183 (2014).
49. J. Ingla-Aynés, M. H. D. Guimarães, R. J. Meijerink, P. J. Zomer, B. J. van Wees, *Phys. Rev. B* **92**, 201410 (2015).
50. L. A. Cohen *et al.*, *Science* **382**, 542–547 (2023).
51. J. Barrier *et al.*, *Nature* **628**, 741–745 (2024).
52. K. Huang, High-Temperature Quantum Valley Hall Effect with Quantized Resistance and a Topological Switch, version 1, Harvard Dataverse (2024); <https://doi.org/10.7910/DVN/TM1VK1>.

#### ACKNOWLEDGMENTS

We thank F. Zhang, K. Yang, Y. Oreg, and N. Schiller for helpful discussions and R. Zhang for the LabVIEW program used in measurements. **Funding:** K.H. and J.Z. are supported by the National Science Foundation (NSF) through grant NSF/DMR-1904986 and the Department of Energy through grant DE-SC0022947. DE-SC0022947 supported a portion of the measurements and data analyses. H.F. acknowledges the support of the Penn State Eberly Research Fellowship and the Kaufman New Initiative research grant no. KA2018-98553 of the Pittsburgh

Foundation. K.W. and T.T. acknowledge support from the JSPS KAKENHI (grant nos. 20H00354, 21H05233, and 23H02052) and the World Premier International Research Center Initiative (WPI), MEXT, Japan. Work performed at the National High Magnetic Field Laboratory was supported by the NSF through NSF/DMR-2128556 and the state of Florida. **Author contributions:** K.H. and J.Z. designed the experiment. K.H. fabricated the devices and made the measurements. H.F. assisted in device fabrication and measurement. K.H. and J.Z. analyzed data. K.W. and T.T. synthesized the h-BN crystals. K.H. and J.Z. wrote the manuscript with input from all authors. **Competing interests:** The authors declare no competing interests. **Data and materials availability:** The data that support the plots within this paper are available from Harvard Dataverse (52). **License information:** Copyright © 2024 the authors, some rights reserved; exclusive licensee American Association for the Advancement of Science. No claim to original US government works. <https://www.science.org/about/science-licenses-journal-article-reuse>

#### SUPPLEMENTARY MATERIALS

[science.org/doi/10.1126/science.adj3742](https://science.org/doi/10.1126/science.adj3742)  
Supplementary Text  
Figs. S1 to S9  
Tables S1 to S3  
References (53, 54)

Submitted 22 June 2023; accepted 8 July 2024  
Published online 18 July 2024  
[10.1126/science.adj3742](https://doi.org/10.1126/science.adj3742)